HHS Public Access

Author manuscript

*Proc Natl Acad Sci U S A*. Author manuscript; available in PMC 2026 May 04.

Published in final edited form as:

*Proc Natl Acad Sci U S A*. 2026 February 03; 123(5): e2518372123. doi:10.1073/pnas.2518372123.

# Subcellular mass spectrometry reveals proteome remodeling in an asymmetrically dividing (frog) embryonic stem cell

**Bowen Shen**[a,1], **Leena R. Pade**[a,1], **Fei Zhou**[a], **Peter Nemes**[a,2]

[a]Department of Chemistry & Biochemistry, University of Maryland, College Park, MD 20742

## Abstract

Subcellular proteomics maps protein localization within restricted domains of a cell, complementing high-resolution imaging by expanding the number of proteins that can be profiled at once. Achieving this at depth from subcellular inputs remains challenging. Here, we advance microprobe capillary electrophoresis–mass spectrometry (CE–MS) with trapped ion mobility spectrometry and data-independent acquisition (diaPASEF) to quantify more than a thousand proteins from opposite poles of an asymmetrically dividing embryonic blastomere in live *Xenopus laevis* embryos. From ~200 pg of HeLa digest—approximately 80% of a cell—the technology identified 1,035 proteins with high reproducibility in quantification (coefficient of variation <15% across technical triplicates). With microprobe sampling in vivo, we quantified 808–1,022 proteins from opposite poles of the dorsal–animal (D1) blastomere before division, and we traced how these spatial distributions are retained or remodeled in the descendant D1.1 (neural-fated) and D1.2 (epidermal-destined) cells. To decouple subcellular distributions from dorsal–ventral axis cues, we perturbed patterning by ultraviolet ventralization. These results establish microprobe CE–MS for deep subcellular proteomics in intact embryos and reveal spatially distinct protein distributions during early fate specification. These spatial proteome differences appear consistent with early lineage tendencies yet precede and likely bias, rather than fix, later fate decisions that depend on gastrula-stage inductive signals.

### Keywords

subcellular; proteomics; blastomere; *Xenopus* ; mass spectrometry

Cells are defined not only by which proteins they express but also by where those proteins reside. Subcellular mapping of protein localization captures cell state; however, available technologies often trade depth for spatial precision. Imaging captures exquisite spatial details but probes only a few targets at a time (reviewed in refs. 1 and 2). Mass spectrometry (MS) can quantify thousands of proteins but has traditionally lacked sensitivity and spatial



[2]To whom correspondence may be addressed. nemes@umd.edu.

[1]B.S. and L.R.P. contributed equally to this work.

Author contributions: P.N. conceptualized the study, designed the research objectives, and interpreted results; B.S., L.R.P., and P.N. developed the experiments; L.R.P. performed biological experiments and collected the cell contents; B.S. developed the analytical method, prepared and measured samples, and, together with L.R.P., analyzed data; F.Z. prepared the spectral library; B.S., L.R.P., and P.N. wrote the draft manuscript; P.N. edited and finalized the report and acquired funding.

The authors declare no competing interest.

context at the scale of tiny cellular niches. Bridging this technological gap remains a key objective in cell biology.

*Xenopus laevis* offers a tractable and robust system for relating molecular organization to fate. Decades of work in this model have defined canonical mechanisms of early development and vertebrate body plan patterning (e.g., reviewed in refs. 3–5). After fertilization, microtubule-driven cortical rotation establishes dorsal–ventral cues, which are refined at gastrulation by bone morphogenetic protein (BMP) signaling. Large cell size, precise manipulability, and stereotyped fates make *Xenopus* especially useful for studies (e.g., reviewed in refs. 6–8). At cleavage, the dorsal–animal (called D1) blastomere (Fig. 1) reproducibly yields offspring cells that contribute to the neural ectoderm (e.g., D1.1, or D11 lineage) or head epidermis (e.g., D1.2, or D12 lineage) (9), yet these tendencies are conditional. For example, the epidermally fated D12 can adopt neural identity when BMP is inhibited, and the neural-destined D11 can become epidermal if inductive cues are absent. Whether asymmetric subcellular protein organization in a precursor such as D1 biases the responses of its descendant cells remains a central question in the molecular logic of cell differentiation.

Single-cell MS has rapidly advanced, increasing proteome depth from individual cells across diverse contexts (e.g., reviewed in refs. 10–12). In *Xenopus* blastomeres, early analyses reported ~800 proteins, (13, 14) rising to ~1,700 proteins with sensitivity gains in capillary electrophoresis (CE) (13–17) and liquid chromatography (LC) (18, 19). Modern single-cell MS can now quantify up to thousands of proteins per mammalian cell, including early metastatic lung cells (20), monocytes/macrophages (21, 22), and neutrophils (23, 24). Patch-clamp proteomics of identified neurons has detected ~160 proteins from the soma (25) and ~1,400 proteins from whole cells (26). Progress toward subcellular proteomics has also accelerated (reviewed in refs. 10 and 27–29). However, many current strategies fractionate large populations, mapping more than 12,000 proteins across 13 organelles (30) or ~7,600 proteins across 19 compartments (31) and tracking dynamics across subcellular compartments (32), while sacrificing single-cell and cell-type specificity (33). Microsampling CE–MS proteomics (15) has partially addressed this challenge by providing access to single cells in tissues (e.g., reviewed in refs. 10, 34, and 35). However, in vivo approaches that sample defined subcellular volumes within identified cells remain limited in terms of proteome depth and throughput, particularly in fast-dividing blastomeres in live embryos.

Here, we develop a minimally invasive, sensitive workflow to profile opposite poles within the same blastomere of live embryos to decipher protein differences during asymmetric division. This report builds on our disclosure of the technology in 2023 (36, 37). Our technological milestone was to advance microprobe CE–MS (15, 16) sensitivity to at least 1,000 proteins in subcellular niches reliably. To mitigate chimeric $MS^2$ spectra encountered previously using orbitrap MS (17), we leverage timsTOF MS (38) features: rapid ion-mobility separation to reduce spectral interference, ion trapping to increase signal accumulation, and full-duty-cycle $MS^2$ for efficient peptide sequencing. We then map how the D1 blastomere proteome is partitioned across opposite poles, test inheritance versus remodeling into the descendant D11 and D12 cells, and assess Spemann’s Organizer

dependence by ultraviolet (UV) ventralization. The resulting in vivo subcellular proteome maps provide a benchmark for targeted functional studies of protein distributions in early embryos, which can be followed up in subsequent investigations.

## Results

Fig. 1 illustrates the integrated biological and analytical workflow. We scaled capillary-microsampling (15) to collect subcellular proteome niches from the D11 and D12 poles within the same D1 blastomere (8-cell stage), respectively referred to as ‘D11 and ‘D12, and from the cytoplasm of the descendant D11 and D12 blastomeres (16-cell stage). Sampling took ~10 s per aspiration in the live embryos, faster than the ~20 min developmental time between the 8- and 16-cell stages at room temperature. The aspirates were processed using a minimal-proteome workflow and analyzed by CE–MS. The proteome profiles were evaluated by established multivariate and statistical analyses. Technical details are in SI Appendix. Because the ‘D11 and D11 lie more dorsally than the ‘D12 and D12, we repeated measurements in UV-ventralized embryos to test dependence on dorsal–ventral patterning. This study was not designed to assign function to individual proteins. The resulting in vivo protein maps provide hypotheses for targeted follow-up experiments. All protein identifications and quantitative values are provided in SI Appendix for transparency and reuse.

### Enhancement of Proteome Sensitivity.

Proteome coverage was the key constraint for subcellular profiling. We benchmarked technical performance using ~200 pg of HeLa proteome digest, equivalent to ~80% of a cell. The samples were analyzed on a validated CE–timsTOF mass spectrometer (15) (SI Appendix, SI Methods). diaPASEF acquisition was optimized using complementary windowing schemes across technical quadruplets: “broad” (*m/z* 400–1,200 Th, 15 m/z windows, 4.80 s cycle time), “wide” (500–1,200 Th, 20, 2.74 s), extra-wide (400–1,200 Th, 25, 2.74 s), and “super-wide” (400–1,600, 50, 2.85 s). The extra-wide scheme yielded the deepest coverage (Fig. 2A). Because library-based DIA can outperform library-free analysis at low input (39), we built a project-specific spectral library from 28 ddaPASEF runs of 10 ng HeLa digest per run (~40 cells) and identified 1,035 proteins in 20-min CE separations.

We quantified 1,015 proteins across technical triplicates from ~200 pg input (Dataset S1). Standard LFQ was performed to estimate protein concentrations (SI Appendix, SI Methods). The median LFQ CV were <15% for all acquisition schemes and for both library-free and library-based processing, indicating high reproducibility (Fig. 2B). Protein abundances from library-based and library-free analyses correlated strongly (Fig. 2C, Pearson $\rho$ = 0.81), revealing robustness, consistent with our recent work (40). Compared with our prior CE–DIA on an orbitrap analyzer (17), CE–diaPASEF on the timsTOF PRO identified ~50% more proteins from single-cell-equivalent digests, broadly extending into the lower-abundance range (Fig. 2D; $P = 9.27 \times 10^{-89}$). With a higher sensitivity, we selected the 25 m/z extra-wide diaPASEF configuration, along with library-based analysis, for all subsequent single-cell and subcellular measurements.

### Exploring Subcellular Proteome Niches.

With the optimized CE–MS configuration, we integrated capillary microsampling to probe subcellular proteome heterogeneity. As shown in Fig. 3A, we microaspirated ~10 nL (~5% volume) from the ‘D11 and ‘D12 within the same D1 blastomere and the ~90 nL cytoplasmic content from the D11 and D12 descendants. The sampling was performed in n = 4 to 5 biological replicates (BRs) per condition, with each sample analyzed in 2 to 3 technical replicates (TRs). The $BR_{TR}$ identities were traced through the study. However, access to this information was blinded during unsupervised analysis and was only revealed for supervised data analyses and to aid in the interpretation of results.

The subcellular samples were processed at ~10- to 100-times lower amounts than typical bottom–up workflows, yielding ~3.5 µL digest per aspirate. Approximately 10 nL of each extract, corresponding to ~0.015% of the D1 proteome, was finally analyzed on the CE–timsTOF platform. We quantified 808 proteins in the ‘D11 and 1,022 in the ‘D12 (Dataset S2). STRING protein–protein interaction analysis of canonical functions revealed enrichment for translation, mitochondrial respiration, glycolysis/gluconeogenesis, proteostasis, amino acid metabolism, protein folding, and nuclear transport, consistent with an active biosynthetic and metabolic organization within discrete subcellular niches.

The protein concentrations were compared. Supervised tests (two-sided Student’s *t* test, $P < 0.05$; fold change > 1.5) identified 158 differences: 27 proteins enriched in the ‘D11 and 131 toward the ‘D12 in the D1 cells. The remaining 755 proteins had comparable abundance (Fig. 3 B, *Top*; and Dataset S3). Unsupervised HCA of the top 45 differentially abundant proteins (Fig. 3 B, *Bottom*; and close-up in SI Appendix, Fig. S1) grouped the samples by pole identity despite information on sample identities being withheld, with two clusters enriched in the ‘D12 (groups #1 and #2) and one in the ‘D11 (group #3). Gene ontology (GO) analysis using PantherDB (41) returned functions enriched in binding (86 proteins), catalytic activity (85 proteins), and structural molecule activity (20 proteins).

We examined representative proteins for canonical roles using Xenbase.org (42) as the search engine. Cytochrome c oxidase subunit 7A2 (Cox7a2) was 5.27-fold higher in the ‘D11 (cluster #3; $P = 0.002$), consistent with roles in mitochondrial respiration (43) and later neural expression at tailbud stages (44). Class II β-tubulin (Tubb2b) was 5.05-fold higher in ‘D11 ($P = 0.0003$), aligning with forebrain expression (45). In contrast, myosin heavy chain 9 (Myh9) was 1.48-fold higher in the ‘D12 ($P = 0.01$), in line with its epidermal expression in zebrafish (46). Additional D12-enriched examples included cathepsin D (Ctsd: 6.02-fold; $P = 0.0016$), eIF2 alpha kinase activator homolog GCN1 (Gcn1: 4.40-fold; $P = 0.005$), and adenosylhomocysteinase (Ahcy: 2.4-fold, $P = 0.01$), all of which are linked to epidermal, retinal, or ectodermal fates (42), a stereotypical destiny of the D12 blastomere lineage (9). These associations provide biological plausibility for the observed spatially distinct protein distributions within a single blastomere; however, they do not assign function at cleavage stages.

### Proteome Remodeling During Asymmetric Division.

We asked whether subcellular differences in the D1 precursor persist in the descendants. We extended microprobe CE–diaPASEF to the descendant D11 and D12 blastomeres in n = 4 to 5 BRs, each from a different embryo, using unpaired statistical tests. The aspirations were conducted in a random order. Approximately 5 ng total protein (~0.03% of the cell proteome) was analyzed per run. We identified 1,220 proteins in D11 and 891 in D12 (Dataset S4). The measured protein LFQ concentrations (Dataset S5) were compared. Most proteins were comparable between the D11 and D12 (864 with $P \geq 0.05$ or fold change < 1.5), while 185 differed significantly. Of these, 114 were higher in the D12 and 71 were higher in D11 blastomeres (Fig. 3 C, *Top*).

Unsupervised HCA of the 45 most differentially abundant proteins separated the two cell types (Fig. 3 C, *Bottom*; and close-up in SI Appendix, Fig. S2). One replicate (sample $1_1$) showed outlier behavior and is annotated in SI Appendix. Group #1 was enriched in the D12 and included yolk-related proteins such as vitellogenin a2 (Vtga2: D12/D11 = 3.09; $P = 0.0001$) and vitellogenin b1 (Vtgb1: D12/D11 = 3.47; $P = 0.0002$). This pattern is consistent with D12's lateral position within the animal tier and with yolk accumulation being highest in ventral–vegetal blastomeres (13, 14, 47). In contrast, Group #2 was enriched in the D11 and included proteins associated with neural development, consistent with the stereotypical fate of this cell type. Examples include programmed cell death protein 4 (Pdcd4: D11/D12 = 2.47; $P = 0.004$), expressed during later neural plate and placode formation (Nieuwkoop–Faber stages 15 to 32) (48), and developmentally regulated GTP-binding protein 1 (Drg1: D11/D12 = 1.56; $P = 0.01$), expressed in the eyes, brain, and spinal cord (49, 50). These associations provide biological context and do not assign function at cleavage stages.

We next compared dorsal-to-near ventral ratios before and after division for proteins measured at both stages. Fig. 4A correlates the 'D11/'D12 ratio at the 8-cell stage with the D11/D12 ratio at the 16-cell stage protein by protein (Dataset S6). Among 829 shared proteins, 517 showed no significant change ($P \geq 0.05$) and clustered near the origin. Thirty-seven differed at both time points and were distributed across four quadrants. Quadrant #1 contained proteins enriched toward the dorsal side before and after division (higher at 'D11 and higher in D11), for example, Cox7a2 and Ras GTPase-activating protein-binding protein 1 (G3bp1) implicated in neural tissues (44) and CNS axon regeneration (51). Quadrant #3 contained proteins enriched toward the near ventral side at both stages (higher at 'D12 and higher in D12), for example, Ctbs associated with endodermal and gut tissues. Quadrants #2 and #4 contained 19 proteins that reversed relative enrichment across division, indicating remodeling; for example, Ras GTPase-activating protein-binding protein 2 (G3bp2), implicated in neuronal maintenance (52), was more abundant at 'D12 but became enriched in the D11. In addition, 152 proteins changed only after division, whereas 123 initially differed but subsequently equalized. These patterns indicate active reorganization of spatially distinct protein distributions during asymmetric division. D11 and D12 remain plastic at gastrulation and depend on inductive cues, particularly BMP signaling (53). We therefore interpret these early differences as molecular biases in competence rather than fixed determinants of fate.

### Functional Test of an Asymmetric Proteome Dowry.

We asked whether early subcellular asymmetries depend on dorsal–ventral patterning. In *Xenopus*, UV irradiation disrupts vegetal-cortex microtubules and blocks cortical rotation, preventing transport of dorsalizing determinants (e.g., Dsh, β-catenin stabilizers) and producing ventralized embryos with reduced head and neural structures and prominent ventral structures like the characteristic “belly piece” (4). As shown in Fig. 4B, 15 of 15 experimental embryos exposed to 90 s UV (UV+) were indistinguishable from the controls (UV–) at stages 5 to 6 (~2 h 15 min postfertilization, pf). By stage 32 (~2 d pf), UV+ tadpoles were severely ventralized, lacking eyes and brain (DAI = 1.5 ± 0.7, SI Appendix), validating the perturbation for functional testing.

Next, we compared the subcellular ratios before and after UV-treatment (n = 4, Fig. 4C) along the dorsal–near ventral direction. We identified 875 proteins in the ‘D11 and 832 in the ‘D12 (Dataset S7); 609 were quantified in both UV− and UV+ conditions (Dataset S8). Unsupervised HCA of the top 50 proteins clustered technical duplicates and separated ‘D11 from ‘D12 (SI Appendix, Fig. S3), indicating that subcellular differences persist even after UV treatment. Across the shared dataset, 467 proteins were unchanged by UV ($P \geq 0.05$). Notably, 118 proteins that differed in UV– became indistinguishable in UV+, consistent with Organizer dependence. For example, Cox7a2 shifted from higher in D11 in the control (D11/D12 = 5.27, $P = 0.002$) to comparable after UV (0.95, $P = 0.617$), as did Tubb2b (ratio from 5.05 to 1.04). In general, a substantially lower number of proteins exhibited differences after UV irradiation (SI Appendix, Fig. S4). STRING analysis linked the UV-sensitive set to amino-acid biosynthesis, respiratory electron transport, fatty-acid degradation, and protein folding.

We also examined the most dorsal niche, the ‘D11, which we anticipated to be most sensitive to ventralization. Of 927 quantified proteins, 734 were unchanged, 83 increased, and 110 decreased after UV (SI Appendix, Fig. S6 and Dataset S9). Ingenuity pathway analysis (IPA) of the downregulated set (SI Appendix, Fig. S7), mapped to human orthologs, indicated reduced categories related to cellular assembly and organization (IPA score 55), cell signaling (score 39), and cell morphology (score 17). Embryonic development and nervous system development were also reduced (score 10). Twenty-seven downregulated proteins had transcripts reported as high in the brain, eye, or spinal cord, which arise from D11 lineage tissues. Examples include Ranbp1, linked to neural crest migration (54) (UV+: D11/D12 = 0.64, $P = 0.04$), and Nap1l1, a regulator of neural progenitor proliferation (55) (0.61, $P = 0.002$). Several 14-3-3 isoforms important for neuronal development (56) (Ywhae, Ywhaq, Ywhaz) also decreased (0.38 to 0.60, $P = 0.002$ to 0.04).

Few differentially regulated proteins are canonical dorsal–ventral components, yet several intersect processes that influence Wnt/BMP signaling and patterning. They include cytoskeletal regulation (Actb), membrane dynamics (Anxa1, Anxa5), chromatin regulation (Asf1a), and energy production (multiple Atp5 subunits). Ubiquitin C-terminal hydrolase L1 (Uchl1), which stabilizes β-catenin by deubiquitination (57), was significantly reduced (UV+: D11/D12 = 0.29, $P = 0.0006$), as was S-phase kinase-associated protein 1 (Skp1), a β-catenin stabilizer with documented roles in neural crest induction (58). These results suggest that ventralization blunts a subset of dorsal-biased proteins and remodels others,

consistent with organizer-dependent control of early proteome organization. We interpret these changes as shifts in competence rather than fixed fate determinants and view them as hypotheses for targeted functional tests.

## Discussion

We established in vivo subcellular MS proteomics for asymmetric division. From ~200 pg of digest, ~80% of a HeLa cell, the workflow consistently identified > 1,000 proteins with median CVs < 15%, with and without a spectral library. The CE–diaPASEF platform maintained this sensitivity for subcellular aspirates from the poles of the D1 blastomere and their descendant whole D11 and D12 offspring. This enabled a direct test of inheritance versus remodeling across division in *X. laevis*.

The results support a competence-based view of early fate specification. UV ventralization blunted a subset of dorsal-biased proteins and equalized others in abundance, indicating dependence on dorsal–ventral patterning. The D11 and D12 cells differed in proteins linked to metabolism, cytoskeleton, and RNA regulation in ways that align with later neural vs. epidermal outcomes. Cleavage-stage blastomeres remain plastic and depend on gastrula-stage induction, particularly BMP antagonism, to realize those outcomes. We therefore interpret early asymmetries as molecular biases that tune responsiveness to induction rather than fixed determinants of fate.

This study was not designed to assign function to individual proteins. Orthogonal validation of localizations and causal tests is the next logical step. Imaging of candidates and perturbations that modulate competence to neural induction would directly evaluate whether early proteomic asymmetries influence lineage decisions. The maps provided here offer rational starting points for such targeted studies.

## Materials and Methods

Full methods are in SI Appendix. All procedures for the humane care and use of *X. laevis* were approved by the University of Maryland Institutional Animal Care and Use Committee (R-FEB-21-07 and R-FEB-24-05). Identified blastomeres were sampled in vivo with precision microcapillaries to aspirate small aliquots from opposite subcellular poles of the same blastomere, followed by a minimal-loss bottom–up proteomics workflow. Proteomes were separated by CE and analyzed by trapped-ion-mobility time-of-flight MS using DIA. BR numbers were set a priori from pilot studies. Each BR was measured in TRs. Statistical controls and data processing are detailed in SI Appendix.

## Supplementary Material

Refer to Web version on PubMed Central for supplementary material.

## ACKNOWLEDGMENTS.

Parts of this work were supported by the Arnold and Mabel Beckman Foundation (Beckman Young Investigator Award to P.N.), the Chan Zuckerberg Initiative (award to P.N.), the National Institute of General Medical Sciences of the NIH (R35GM124755 to P.N.), or the COSMOS Club Foundation (fellowship to B.S.). The views expressed

in this publication are those of the authors and do not necessarily reflect the sponsors. We thank Md. Tarikul Islam (University of Maryland, College Park, MD) for assistance with data analysis using IPA.

## Data, Materials, and Software Availability.

Primary MS data, spectral libraries, and reference proteomes were deposited in the Proteomics Identifications Database under PXD063566 (59). All other data are included in the manuscript and/or supporting information.

## References

1. Liu S, Hoess P, Ries J, Super-resolution microscopy for structural cell biology. Ann. Rev. Biophys 51, 301–326 (2022). [PubMed: 35119945]
2. Cheng YF, Single-particle cryo-EM-How did it get here and where will it go. Science 361, 876–880 (2018). [PubMed: 30166484]
3. Gerhart J et al. , Cortical rotation of the *Xenopus* egg—Consequences for the anteroposterior pattern of embryonic dorsal development. Development 107, 37–51 (1989). [PubMed: 2699856]
4. Harland R, Gerhart J, Formation and function of Spemann's organizer. Annu. Rev. Cell Dev. Biol 13, 611–667 (1997). [PubMed: 9442883]
5. De Robertis EM, Larraín J, Oelgeschläger M, Wessely O, The establishment of Spemann's organizer and patterning of the vertebrate embryo. Nat. Rev. Genet 1, 171–181 (2000). [PubMed: 11252746]
6. Moody SA, Bauer DV, Hainski AM, Huang S, "Determination of Xenopus cell lineage by maternal factors and cell interactions" in Current Topics in Developmental Biology, Pedersen RA, Schatten GP, Eds. (Elsevier Academic Press Inc., San Diego, CA, 1996), vol. 32, pp. 103–110. [PubMed: 8929667]
7. Kumano G, Smith WC, Revisions to the *Xenopus* gastrula fate map: Implications for mesoderm induction and patterning. Dev. Dyn 225, 409–421 (2002). [PubMed: 12454919]
8. Lane MC, Sheets MD, Heading in a new direction: Implications of the revised fate map for understanding *Xenopus laevis* development. Dev. Biol 296, 12–28 (2006). [PubMed: 16750823]
9. Moody SA, Fates of the blastomeres of the 16-cell stage *Xenopus* embryo. Dev. Biol 119, 560–578 (1987). [PubMed: 3803718]
10. Pade LR, Stepler KE, Portero EP, DeLaney K, Nemes P, Biological mass spectrometry enables spatiotemporal'omics: From tissues to cells to organelles. Mass Spectrom. Rev 43, e21824 (2023).
11. Guo TN, Steen JA, Mann M, Mass-spectrometry-based proteomics: From single cells to clinical applications. Nature 638, 901–911 (2025). [PubMed: 40011722]
12. Sanchez-Avila X, de Oliveira RM, Huang S, Wang C, Kelly RT, Trends in mass spectrometry-based single-cell proteomics. Anal. Chem 97, 5893–5907 (2025). [PubMed: 40091206]
13. Lombard-Banek C, Moody SA, Nemes P, Single-cell mass spectrometry for discovery proteomics: Quantifying translational cell heterogeneity in the 16-cell frog (*Xenopus*) embryo. Angew. Chem. Int. Ed 55, 2454–2458 (2016).
14. Lombard-Banek C, Reddy S, Moody SA, Nemes P, Label-free quantification of proteins in single embryonic cells with neural fate in the cleavage-stage frog (*Xenopus laevis*) embryo using capillary electrophoresis electrospray ionization high-resolution mass spectrometry (CE-ESI-HRMS). Mol. Cell. Proteomics 15, 2756–2768 (2016). [PubMed: 27317400]
15. Lombard-Banek C et al. , In vivo subcellular mass spectrometry enables proteo-metabolomic single-cell systems biology in a chordate embryo developing to a normally behaving tadpole (*X. laevis*). Angew. Chem. Int. Ed 60, 12852–12858 (2021).
16. Lombard-Banek C, Moody SA, Manzini MC, Nemes P, Microsampling capillary electrophoresis mass spectrometry enables single-cell proteomics in complex tissues: Developing cell clones in live *Xenopus laevis* and zebrafish embryos. Anal. Chem 91, 4797–4805 (2019). [PubMed: 30827088]

17. Shen B, Chen J, Nemes P, Electrophoresis-correlative data-independent acquisition (Eco-DIA) improves the sensitivity of mass spectrometry for limited proteome amounts. Anal. Chem 96, 15581–15587 (2024). [PubMed: 39292951]
18. Sun L et al. , Single cell proteomics using frog (*Xenopus laevis*) blastomeres isolated from early stage embryos, which form a geometric progression in protein content. Anal. Chem 88, 6653–6657 (2016). [PubMed: 27314579]
19. Saha-Shah A et al. , Single cell proteomics by data-independent acquisition to study embryonic asymmetry in *Xenopus laevis*. Anal. Chem 91, 8891–8899 (2019). [PubMed: 31194517]
20. Tsai CF et al. , Surfactant-assisted one-pot sample preparation for label-free single-cell proteomics. Commun. Biol 4, 265 (2021). [PubMed: 33649493]
21. Budnik B, Levy E, Harmange G, Slavov N, SCoPE-MS: Mass spectrometry of single mammalian cells quantifies proteome heterogeneity during cell differentiation. Genome Biol 19, 161 (2018). [PubMed: 30343672]
22. Specht H et al. , Single-cell proteomic and transcriptomic analysis of macrophage heterogeneity using SCoPE2. Genome Biol 22, 50 (2021). [PubMed: 33504367]
23. Shen B et al. , Rapid CE–MS with real-time Eco–AI resolves proteomic heterogeneity among single human neutrophils. bioRxiv [Preprint] (2025). 10.1101/2025.08.14.670204 (Accessed 9 January 2026).
24. Sadiku P et al. , Single cell proteomic analysis defines discrete neutrophil functional states in human glioblastoma. bioRxiv [Preprint] (2025). 10.1101/2025.07.23.666094 (Accessed 9 January 2026).
25. Choi SB, Polter AM, Nemes P, Patch-clamp proteomics of single neurons in tissue using electrophysiology and subcellular capillary electrophoresis mass spectrometry. Anal. Chem 94, 1637–1644 (2022). [PubMed: 34964611]
26. Ghatak S et al. , Single-cell patch-clamp/proteomics of human Alzheimer's disease iPSC-derived excitatory neurons versus isogenic wild-type controls suggests novel causation and therapeutic targets. Adv. Sci 11, 2400545 (2024).
27. Dreger M, Subcellular proteomics. Mass Spectrom. Rev 22, 27–56 (2003). [PubMed: 12768603]
28. Yates JR, Gilchrist A, Howell KE, Bergeron JJM, Proteomics of organelles and large cellular structures. Nat. Rev. Mol. Cell Biol 6, 702–714 (2005). [PubMed: 16231421]
29. Nemes P, Mass spectrometry comes of age for subcellular organelles. Nat. Methods 18, 1157–1158 (2021). [PubMed: 34608316]
30. Thul PJ et al. , A subcellular map of the human proteome. Science 356, eaal3321 (2017).
31. Hein MY et al. , Global organelle profiling reveals subcellular localization and remodeling at proteome scale. Cell 188, 1137–1155 (2025). [PubMed: 39742809]
32. Martinez-Val A et al. , Spatial-proteomics reveals phospho-signaling dynamics at subcellular resolution. Nat. Commun 12, 7113 (2021). [PubMed: 34876567]
33. Arslan T et al. , SubCellBarCode: Integrated workflow for robust spatial proteomics by mass spectrometry. Nat. Protoc 17, 1832–1867 (2022). [PubMed: 35732783]
34. Lombard-Banek C, Portero EP, Onjiko RM, Nemes P, New-generation mass spectrometry expands the toolbox of cell and developmental biology. Genesis 55, e23012 (2017).
35. Portero EP, Pade LR, Li J, Choi SB, Nemes P, "Single-cell mass-spectrometry of metabolites and proteins for systems and functional biology" in Neuromethods, Sweedler JV, Eberwine JH, Fraser SE, Eds. (Humana Press, New York, NY, 2023), vol. 184, pp. 87–114.
36. Shen B, Pade LR, Nemes P, American Society for Mass Spectrometry (American Chemical Society, Houston, TX, 2023).
37. Shen B, Pade LR, Zhou F, Nemes P, US Human Proteome Organization (HUPO, Chicago, IL, 2023).
38. Meier F et al. , DiaPASEF: Parallel accumulation–serial fragmentation combined with data-independent acquisition. Nat. Methods 17, 1229–1236 (2020). [PubMed: 33257825]
39. Wen CW et al. , Investigation of effects of the spectral library on analysis of diaPASEF data. J. Proteome Res 21, 507–518 (2022). [PubMed: 34969243]

40. Shen B, Pade L, Nemes P, Data-independent acquisition shortens the analytical window of single-cell proteomics to fifteen minutes in capillary electrophoresis mass spectrometry. J. Proteome Res 23, 692–703 (2025).
41. Mi HY et al. , PANTHER version 16: A revised family classification, tree-based classification tool, enhancer regions and extensive API. Nucleic Acids Res 49, D394–D403 (2021). [PubMed: 33290554]
42. Fisher M et al. , Xenbase: key features and resources of the Xenopus model organism knowledgebase. Genetics 224, iyad018 (2023).
43. Bateman A et al. , UniProt: The universal protein knowledgebase in 2023. Nucleic Acids Res 51, D523–D531 (2023). [PubMed: 36408920]
44. Pollet N et al. , An atlas of differential gene expression during early *Xenopus* embryogenesis. Mech. Dev 122, 365–439 (2005). [PubMed: 15763213]
45. Daume D, Offner T, Hassenklöver T, Manzini I, Patterns of tubb2b promoter-driven fluorescence in the forebrain of larval *Xenopus laevis*. Front. Neuroanat 16, 914281 (2022). [PubMed: 35873659]
46. Huang Y et al. , Nonmuscle myosin II-B (myh10) expression analysis during zebrafish embryonic development. Gene Expr. Patterns 13, 265–270 (2013). [PubMed: 23665442]
47. Miller JR et al. , Establishment of the dorsal-ventral axis in *Xenopus* embryos coincides with the dorsal enrichment of dishevelled that is dependent on cortical rotation. J. Cell Biol 146, 427–438 (1999). [PubMed: 10427095]
48. Zhang Z et al. , Similarity in gene-regulatory networks suggests that cancer cells share characteristics of embryonic neural cells. J. Biol. Chem 292, 12842–12859 (2017). [PubMed: 28634230]
49. Ishikawa K et al. , Cloning and characterization of *Xenopus laevis* drg2, a member of the developmentally regulated GTP-binding protein subfamily. Gene 322, 105–112 (2003). [PubMed: 14644502]
50. Kumar S, Iwao M, Yamagishi T, Noda M, Asashima M, Expression of GTP-binding protein gene drg during *Xenopus laevis* development. Int. J. Dev. Biol 37, 539–546 (1993). [PubMed: 8179998]
51. Sahoo PK et al. , Disruption of G3BP1 granules promotes mammalian CNS and PNS axon regeneration. Proc. Natl. Acad. Sci. U.S.A 122, e2411811122 (2025). [PubMed: 40014573]
52. Sidibé H, Dubinski A, Vande Velde C, The multi-functional RNA-binding protein G3BP1 and its potential implication in neurodegenerative disease. J. Neurochem 157, 944–962 (2021). [PubMed: 33349931]
53. HemmatiBrivanlou A, Melton D, Vertebrate embryonic cells will become nerve cells unless told otherwise. Cell 88, 13–17 (1997). [PubMed: 9019398]
54. Barriga EH, Alasaadi DN, Mencarelli C, Mayor R, Pichaud F, Ranbp1 plays an essential role in directed migration of neural crest cells during development. Dev. Biol 492, 79–86 (2022). [PubMed: 36206829]
55. Wischnewski J, Sölter M, Chen Y, Hollemann T, Pieler T, Structure and expression of *Xenopus* karyopherin-β3: Definition of a novel synexpression group related to ribosome biogenesis. Mech. Dev 95, 245–248 (2000). [PubMed: 10906471]
56. Torrico B et al. , Involvement of the 14-3-3 gene family in autism spectrum disorder and schizophrenia: Genetics, transcriptomics and functional analyses. J. Clin. Med 9, 1851 (2020). [PubMed: 32545830]
57. Song J et al. , A protein interaction between β-catenin and Dnmt1 regulates Wnt signaling and DNA methylation in colorectal cancer cells. Mol. Cancer Res 13, 969–981 (2015). [PubMed: 25753001]
58. Wang Y et al. , *Xenopus* skip modulates Wnt/β-catenin signaling and functions in neural crest induction. J. Biol. Chem 285, 10890–10901 (2010). [PubMed: 20103590]
59. Shen B, Pade LR, Zhou F, Nemes P, Subcellular mass spectrometry reveals proteome remodeling in an asymmetrically dividing (frog) embryonic stem cell. PRIDE. https://www.ebi.ac.uk/pride/archive/projects/PXD063566. Deposited 2 May 2025.

## Significance

Asymmetric division partitions molecules into restricted cellular domains that shape future identities, yet protein profiling in these domains has been limited. We introduce a microprobe capillary electrophoresis ion mobility mass spectrometry workflow that quantifies over one thousand proteins from opposite poles of a single *Xenopus laevis* blastomere before it divides to offspring cells with different tissue fates. The maps reveal spatially distinct protein distributions associated with neural and epidermal trajectories and show partial disruption after perturbation of dorsal to ventral patterning. Because these cell fates remain plastic at gastrulation, we interpret the asymmetries as molecular biases that may shape competence to induction rather than deterministic markers.

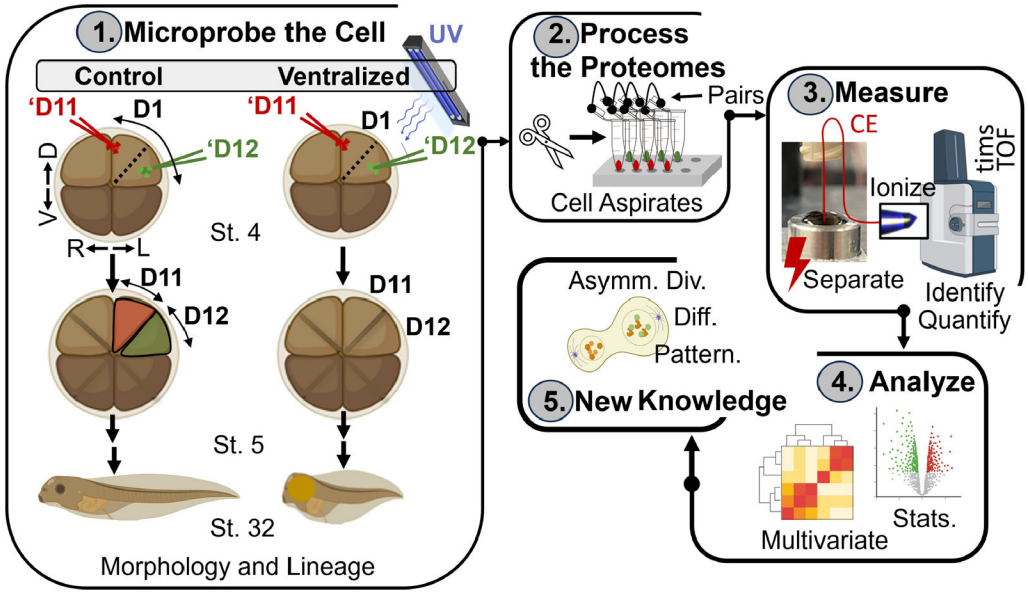


**Fig. 1.**

Live-embryo workflow for subcellular proteomics during asymmetric division. We capillary-microaspirated ~10 nL (~5%) from the ‘D11 (midline) and ‘D12 (lateral) poles within the same dorsal–animal (D1) blastomere of 8-cell *X. laevis* embryos, then sampled the cytoplasm (~90 nL) of the descendant D11 and D12 blastomeres at the 16-cell stage. The proteomes were processed and measured by CE–MS on a timsTOF PRO mass spectrometer optimized for sensitivity (tuned with ~200 pg HeLa proteome digest; SI Appendix, SI Methods). The proteome profiles were quantified and analyzed using multivariate and statistical chemometrics. Dependence on dorsal–ventral patterning was tested by ultraviolet (UV) ventralization. The resulting in vivo maps reveal spatially distinct protein distributions and their remodeling across division (partially created with BioRender).

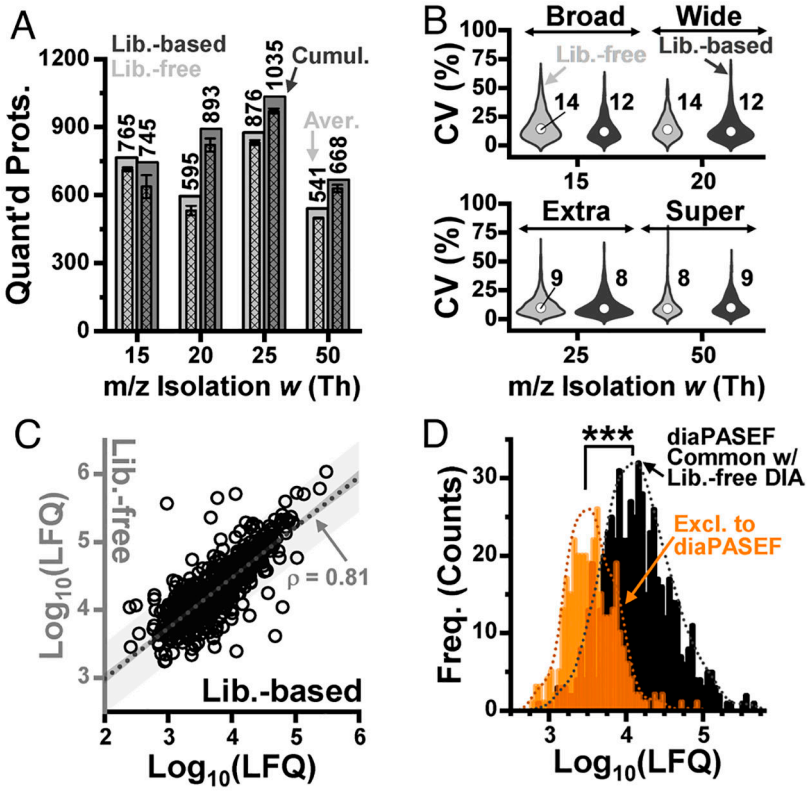


**Fig. 2.**

Tuning CE–diaPASEF for sensitivity on low-input proteomes. Ca. 200 pg HeLa proteome digest (~0.8 cell) was analyzed to benchmark acquisition schemes. Four diaPASEF windowing strategies were tested: broad (scan *m/z* 400–1,200 Th, 15 Th windows isolation, 4.80 s cycle), wide (*m/z* 500–1,200 Th, 20 windows, 2.74 s), extra-wide (*m/z* 400–1,200 Th, 25 windows, 2.74 s), and super-wide (*m/z* 400–1,600 Th, 50 windows, 2.85 s). (*A*) Protein identifications for library-based and library-free processing; the extra-wide yielded the deepest coverage. (*B*) Label-free quantification (LFQ) reproducibility across the schemes, shown as coefficient of variation (CV); median CV < 15% for both processing modes. (*C*) Correlation of protein abundances from library-based vs. library-free analyses using the extra-wide scheme (Pearson ρ = 0.81). (*D*) Sensitivity gain relative to our prior CE-DIA method: proteins uniquely quantified by CE–diaPASEF occupy the lower end of the abundance range. Statistics are two-sided; see SI Appendix, SI Methods. Key: ****P* < 0.001, Mann–Whitney.

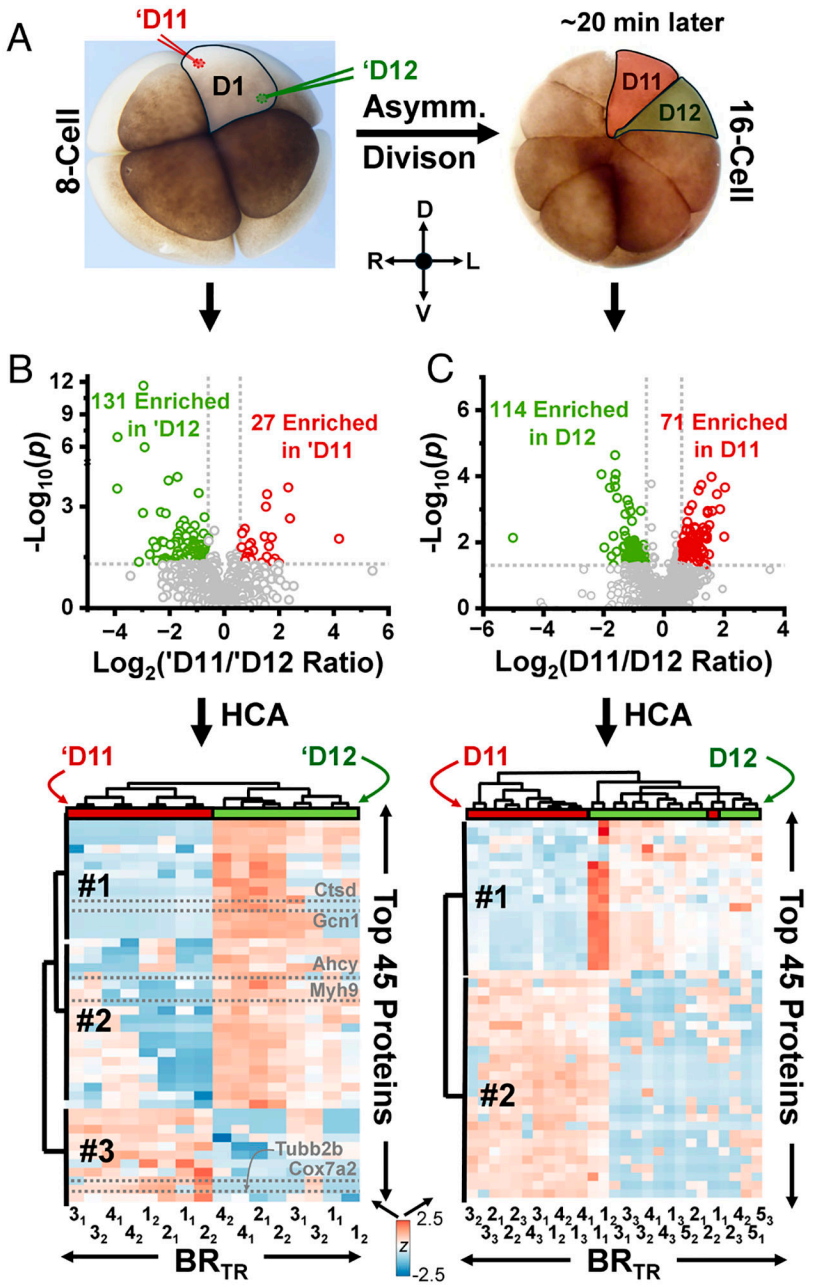


**Fig. 3.**

Subcellular and whole-cell proteome profiling across asymmetric division. (*A*) Sampling scheme. Within the same dorsal–animal (D1) blastomere at the 8-cell stage, ~10 nL (~5%) was microaspirated from the D11 (midline) pole (‘D11) and D12 (lateral) pole (‘D12). At the 16-cell stage, the ~90 nL cytoplasm of the descendant D11 and D12 blastomeres were microsampled. (*B*) Quantitative protein profiling between the subcellular poles (8-cell). *Top*: two-sided Student’s *t* test of protein concentrations comparing ‘D11 vs. ‘D12. 158 proteins differ (27 higher toward ‘D11, 131 toward ‘D12). 755 are comparable. Bottom: unsupervised hierarchical cluster analysis (HCA) of the top 45 differences separates ‘D11 and ‘D12 poles (close-up in SI Appendix, Fig. S1). Heat-map clusters are annotated as groups #1 to #3. (*C*)

Quantitative profiling between the whole blastomeres (16-cell). *Top*: two-sided Student's *t* test comparing the D11 vs. D12. 185 proteins differ (71 higher in D11, 114 in D12). 864 are comparable (close-up in SI Appendix, Fig. S2). Bottom: unsupervised HCA separates the cell types (outlier: $1_1$ sample). Samples are labeled in the $BR_{TR}$ format (BR, biological replicate embryo; TR, technical replicate). Significance threshold (dashed lines) $P < 0.05$ (horizontal) with fold-change > 1.5 (vertical) unless noted.

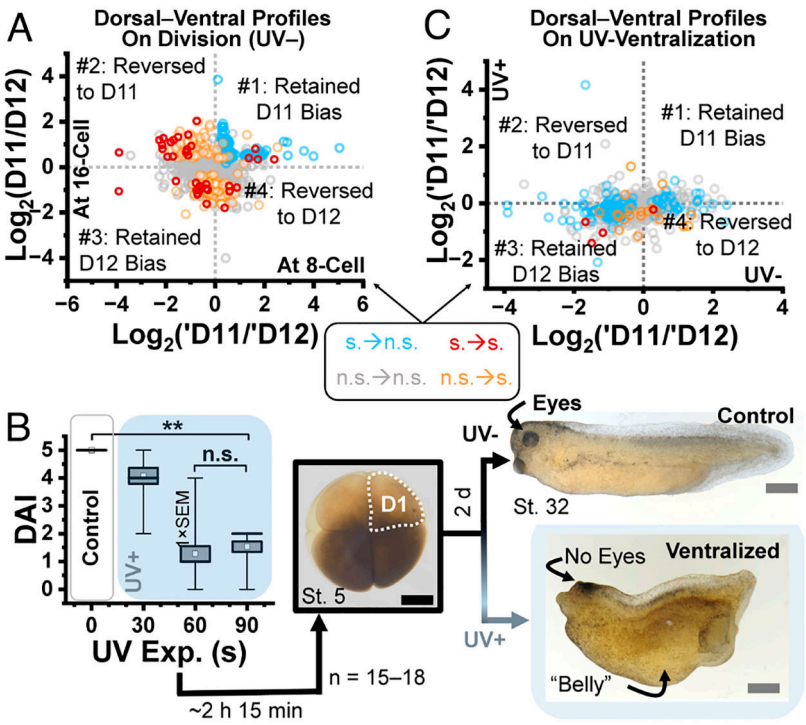


**Fig. 4.**

Effect of ventralization on spatial proteome differences. (*A*) Control (UV−). For each protein quantified at both stages, the ratio is plotted between the D11/D12 poles ('D11/'D12) at the 8-cell stage vs the descendant D11/D12 cells at the 16-cell stage (data in Dataset S8). Positive values indicate higher at 'D11 or in D11; negative values indicate higher at'D12 or in D12 (ventral/lateral). Dashed lines mark no change on both axes. Key to data color code: gray, not significant (n.s., two-tailed Student's *t* test)) at either stage ($P \geq 0.05$ or |fold change| < 1.5); red, significant (s.) at both stages (s.→s.); blue, significant between the poles but not after division (s.→n.s.); orange not significant at the poles but becomes significant after division (n.s.→s.). (*B*) Same analysis after 90 s UV ventralization (UV+). Same key to data color code used; for example, proteins that were significant between dorsal–ventral in UV− and become not significant in UV+ are highlighted in blue, indicating organizer dependence. (*C*) Morphological UV treatment validation (N = 15 to 18 tested). Dorsal–anterior index (DAI) boxplots for UV− and UV+ embryos and early-stage morphology (Nieuwkoop–Faber stage 5) show comparable cleavage. DAI: 1, complete ventralization; 5, none. Representative tadpoles at stage 32 show severe ventralization with UV+ (no eyes/brain; "belly piece"). Key: SEM, standard error of the mean (1× displayed). [Scale bars, 250 μm (black), 1 mm (gray).]